Improving phase estimation using number-conserving operations

Huan Zhang,[1] Wei Ye,[1,2,*] Chaoping Wei,[3] Cunjin Liu,[1] Zeyang Liao,[4,†] and Liyun Hu[1,‡]

[1] *Center for Quantum Science and Technology, Jiangxi Normal University, Nanchang 330022, China*
[2] *School of Computer Science and Engineering, Central South University, Changsha 410083, China*
[3] *Key Laboratory of Water Information Cooperative Sensing and Intelligent Processing, Nanchang Institute of Technology, Nanchang 330022, China*
[4] *School of Physics, Sun Yat-sen University, Guangzhou 510275, China*

(Received 16 December 2020; revised 4 April 2021; accepted 22 April 2021; published 5 May 2021)

We propose a theoretical scheme to improve the resolution and precision of phase measurement with parity detection by using a nonclassical state generated by applying a number-conserving generalized superposition of products (GSP) operation, $(saa^\dagger + ta^\dagger a)^m$ with $s^2 + t^2 = 1$, on a two-mode squeezed vacuum (TMSV) state as the input of Mach-Zehnder interferometer. Then, the statistical properties of the proposed GSP-TMSV are investigated via average photon number (APN), antibunching effect, and two-mode squeezing. Particularly, both higher order m GSP operation and lower proportion parameter s are beneficial for presenting larger total APN, which leads to the improvement of quantum Fisher information (QFI). In addition, we also compare the phase measurement precisions with and without photon losses between our scheme and the previous photon subtraction or photon addition schemes. It is found that our scheme, especially for the case of $s = 0$, even in the presence of photon losses, has the best performance via the enhanced phase resolution, sensitivity, and QFI when compared to those previous schemes. Interestingly, without losses, the standard quantum-noise limit (SQL) is always broken through for our scheme and the phase uncertainty associated with the state of our scheme is closer to the corresponding Heisenberg limit (HL) than the TMSV in the larger total APN region, especially for the case of two-side GSP operation $(m, n) \in (1, 1)$. However, in the presence of photon losses, the HL cannot be beaten, but the SQL can be broken through, particularly for the large total APN regimes.

DOI: 10.1103/PhysRevA.103.052602

I. INTRODUCTION

The ultimate aim of quantum metrology is to achieve higher precision and sensitivity of the phase estimation using (non)classical field of light as the input of optical interferometers [1–4]. Among them, the Mach-Zehnder interferometer (MZI) is one of the most practical interferometers, and its phase sensitivity is limited by standard quantum-noise limit (SQL) $\Delta\varphi = 1/\sqrt{N}$ (N is the average number of photons inside the interferometer), together with solely classical resources as the input of the MZI [5]. In order to go beyond this limit, both the nonclassical states [6,7] and the entangled states [2,8,9] are applied to quantum metrology, which results in the reduction of the phase uncertainty, thereby reaching the Heisenberg limit (HL) $\Delta\varphi = 1/N$ [10]. For instance, Dowling *et al.* [2] pointed out that the so-called N00N states in quantum optical interferometry can achieve the HL. Unfortunately, these states are extremely sensitive to photon losses [9–11]. To solve this problem, Anisimov *et al.* [8] theoretically studied that using the two-mode squeezed vacuum state (TMSV) as the input of the MZI with parity detection scheme, which makes the phase sensitivity exceed the HL. However, restricted by current experimental techniques, it is still difficult to generate strongly entangled TMSV in which its maximum obtainable degree is about $r = 1.15$ ($\bar{n} = \sinh^2 r \approx 2$) [12]. Thus, how to prepare highly nonclassical and strongly entangled quantum states has become one of the most important topics.

For this purpose, the usage of non-Gaussian operations [13–22] is a feasible method, e.g., photon subtraction (PS) [13], photon addition (PA) [16–20], and their superposition [21,22], which also plays an vital role in quantum illumination [23,24], quantum cryptography [25–29], and quantum teleportation [30–32]. For instance, Agarwal and Tara proposed that employing the PA operation to coherent states can transform classical coherent states into highly nonclassical quantum states [16] and this PA operation can be implemented experimentally, proposed by Zavatta [17]. In addition, the PA (or PS) squeezed states have been proved to show the highly nonclassicality [33,34]. Based on these merits mentioned above, Gerry *et al.* [6] proposed a theoretical scheme of simultaneously subtracting the same number of photons from the TMSV (say, PS-TMSV) as the input of the MZI, and showed that the phase measurement uncertainty of the PS-TMSV scheme is smaller than that of the TMSV one for the same squeezing parameters. Then, Ouyang *et al.* [20] used the PA-TMSV as the input state of the MZI, and compared it with both the PS-TMSV and the TMSV under the same squeezing parameters. It is shown that the phase measurement precision

*yeweicsu@csu.edu.cn
†liaozy7@mail.sysu.edu.cn
‡hlyun@jxnu.edu.cn

of the PA-TMSV has a better performance when fixing a small phase shift. In addition to the aforementioned typical non-Gaussian operations, here we suggest a non-Gaussian operation, the number-conserving generalized superposition of products (GSP) operation ($saa^\dagger + ta^\dagger a$) with $s^2 + t^2 = 1$, to operate on the TMSV as the input of the MZI in an attempt to further enhance the resolution and sensitivity of the phase estimation. Besides, the PA-then-PS ($aa^\dagger$) and the PS-then-PA ($a^\dagger a$) are used as special cases of GSP operation to improve entanglement and fidelity of quantum teleportation, but none of them are used to improve phase measurement accuracy, so our scheme in this sense has universality. Not only can this GSP operation be implemented experimentally, as proposed by Kim [35], but also the GSP operation on the TMSV is able to generate a strongly entangled non-Gaussian state as well [36,37].

In order to extract quantum phase information more effectively, three types of detection schemes are usually required, including intensity detection [38,39], homodyne detection [40], and parity detection [41,42]. It should be noted that not all detection schemes can employ the full potential of nonclassical states to achieve superresolution and supersensitivity. In particular, as referred to Ref. [43], intensity detection is more suitable for optical interferometers with coherent light as input, but it is not applicable to the TMSV. To solve this problem, parity detection is a promising candidate, allowing better than classical resolution while keeping the SQL phase sensitivity [44,45]. Thus, taking advantage of parity detection to extract phase information, in this paper, we mainly study the phase resolution and sensitivity of the MZI by using the GSP-TMSV as the input. The numerical simulation results show that our scheme, especially for the case of the PS-then-PA TMSV ($s = 0$), is always superior to the original TMSV scheme with respect to the quantum Fisher information (QFI) and the phase resolution and sensitivity. Additionally, the phase uncertainty associated with the state of our scheme is closer to the corresponding HL than the TMSV in the larger total average photon number (APN) region, especially for the case of two-side GSP operation $(m, n) \in (1, 1)$. Further, from a practical point of view, we also investigate the effects of GSP operations against the photon losses placed in front of parity detection (denoted as an external loss) and between the phase shifter and the second beam splitter (BS) (denoted as an internal loss) because the interaction with the environment is inevitable. Our results show that in the presence of photon losses the phase sensitivity with the GSP-TMSV, especially for the case of $s = 0$, can be still better than that with both the TMSV and the PA(PS)-TMSV under the same accessible parameters. Interestingly, we also find that the effects of the external losses on phase uncertainty are more serious than the internal-loss cases.

The structure of this paper is as follows: In Sec. II, we briefly outline the preparation of the GSP-TMSV state and then present its nonclassicality according to APN, antibunching effect, and two-mode squeezing property. In Sec. III, we show the application of the GSP-TMSV in the MZI and mainly focus on its QFI behavior. After the resolution and sensitivity of phase estimation with parity detection are further discussed in Sec. IV, in Sec. V, we mainly pay attention to the effects of photon losses, involving external and internal losses,

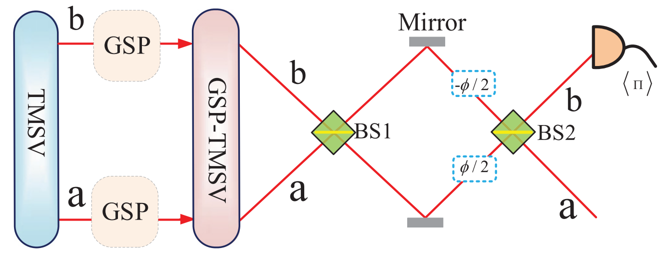

FIG. 1. Schematic diagram of a balanced MZI for the detection of the phase shift (violet) when the GSP-TMSV state is sent to the first BS (green), and the photon-number parity measurements are performed on the output b mode.

on the resolution and sensitivity. Finally, the main results are summarized in Sec. VI.

II. THE GENERATION OF THE GSP-TMSV AND NONCLASSICAL PROPERTIES

In this section, we first introduce the GSP-TMSV in theory and then show its nonclassicality by means of APN, antibunching effect, and two-mode squeezing property.

A. The generation of the GSP-TMSV

In recent years, it has been demonstrated that both the PS-TMSV and the PA-TMSV as the inputs of the MZI can improve the phase sensitivity effectively [6,20], since these non-Gaussian states have the advantages over the Gaussian states in terms of the nonclassicality and the entanglement degree. In this section, we introduce a different kind of non-Gaussian state, the GSP-TMSV, which can be prepared by two GSP operations on the TMSV, as pictured in Fig. 1 (orange box). As referred to in Refs. [36,37], this GSP operation can be seen as an equivalent operator,

$$\hat{O} = (s_1 aa^\dagger + t_1 a^\dagger a)^m (s_2 bb^\dagger + t_2 b^\dagger b)^n, \tag{1}$$

where $s_i^2 + t_i^2 = 1$ $(i = 1, 2)$ and both a $(a^\dagger)$ and b $(b^\dagger)$ are annihilation (creation) operators for modes a and b, respectively. Note that (m, n) represent m-order operation of $s_1 aa^\dagger + t_1 a^\dagger a$ on mode a and n-order operation of $s_2 bb^\dagger + t_2 b^\dagger b$ on mode b. Thus, the GSP-TMSV can be given by

$$\begin{aligned} |\psi\rangle_{ab} &= \frac{\hat{O} S_2(z)}{\sqrt{P_d}} |00\rangle \\ &= \frac{\text{Re}u}{\sqrt{P_d}} \exp(v a^\dagger b^\dagger)|00\rangle, \end{aligned} \tag{2}$$

with

$$\begin{aligned} \text{Re} &= \frac{\partial^{m+n}}{\partial \tau_1^m \partial \tau_2^n} \{\cdot\}|_{\tau_1=\tau_2=0}, \\ u &= \sqrt{1 - z^2} \exp(s_1 \tau_1 + s_2 \tau_2), \\ v &= z \exp(s_1 \tau_1 + t_1 \tau_1 + s_2 \tau_2 + t_2 \tau_2), \end{aligned} \tag{3}$$

where $S_2(z) = \exp[(a^\dagger b^\dagger - ab)\text{arctanh } z]$ is the two-mode squeezing operator with a squeezing parameter z and P_d is a normalization coefficient which can be calculated as

$$P_d = \widetilde{\mathrm{Re}} \frac{uu_1}{1 - vv_1}, \quad (4)$$

with

$$\widetilde{\mathrm{Re}} = \frac{\partial^{2m+2n}}{\partial \tau_1^m \partial \tau_2^n \partial \tau_3^m \partial \tau_4^n} \{\cdot\}|_{\tau_1=\tau_2=\tau_3=\tau_4=0},$$
$$u_1 = \sqrt{1 - z^2} \exp(s_1\tau_3 + s_2\tau_4),$$
$$v_1 = z \exp(s_1\tau_3 + t_1\tau_3 + s_2\tau_4 + t_2\tau_4). \quad (5)$$

It should be emphasized that for simplicity, all the following simulations are based on the assumption of $s_1 = s_2 = s$, $t_1 = t_2 = t$. In particular, when $s = 0$, 0.5, and 1, from Eqs. (1) and (2), one can obtain the PS-then-PA TMSV, a general GSP-TMSV, and the PA-then-PS TMSV, respectively.

For the sake of analysis in the following, here we present the expectation value of a general quantum operator

$$\langle a^l b^k a^{\dagger h} b^{\dagger g} \rangle = \widetilde{\mathrm{Re}} \widetilde{D} P_d^{-1} uu_1 \Delta e^{\Delta w}, \quad (6)$$

with

$$\widetilde{D} = \frac{\partial^{l+k+h+g}}{\partial \tau_5^l \partial \tau_6^k \partial \tau_7^h \partial \tau_8^g} \{\cdot\}|_{\tau_5=\tau_6=\tau_7=\tau_8=0},$$
$$\Delta = (1 - vv_1)^{-1},$$
$$w = \tau_7\tau_8 v_1 + \tau_6\tau_5 v + \tau_6\tau_8 + \tau_5\tau_7, \quad (7)$$

where $l, k, h,$ and g are integers ($\geqslant 0$), Eq. (6) can be used to calculate some expectation values, such as $\langle aa^\dagger \rangle$, $\langle bb^\dagger \rangle$, $\langle aa^\dagger bb^\dagger \rangle$, $\langle a^2 b^{\dagger 2} \rangle$, and $\langle a^{\dagger 2} b^2 \rangle$. The detailed derivation of Eqs. (2) and (6) is shown in Appendix A.

B. Statistical properties of the GSP-TMSV

As described in Refs. [6,7], the nonclassical states of optical field offer a significant improvement in the sensitivity and precision of the MZI, thereby promoting the development of quantum metrology. Before investigating how the GSP-TMSV as the input affects the sensitivity and resolution of the MZI, let us first examine its statisticality in terms of APN, antibunching effect, and two-mode squeezing property, which provide the basis for the performance improvement of the phase estimation in next section.

1. Average photon number

As one of statistical properties of the light field, the APN is an important factor for optical interferometry. In addition, as a kind non-Gaussian operation, the PS from squeezed vacuum state presents an interesting effect of increasing the APN, by which the phase sensitivity can be improved. Here, we first pay attention to the APN and examine if the GSP operation can also increase it. According to Eq. (6), the APN, say, for mode a, can be calculated as

$$\overline{N}_a = \langle a^\dagger a \rangle = \langle aa^\dagger \rangle - 1$$
$$= \frac{\widetilde{\mathrm{Re}}\, uu_1}{P_d} \frac{\partial^2}{\partial \tau_5 \partial \tau_7} \Delta e^{\Delta \tau_5 \tau_7}|_{\tau_5=\tau_7=0} - 1. \quad (8)$$

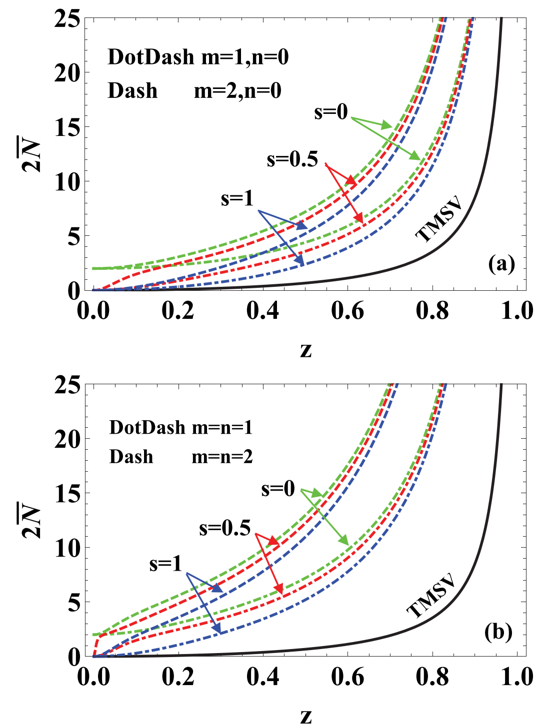

FIG. 2. Average photon number as a function of squeezing parameter z for different operator parameters $s = 0, 0.5, 1$ for (a) single-side GSP operations [$(m, n) \in \{(1, 0), (2, 0)\}$] and (b) two-side symmetric GSP operations [$(m, n) \in \{(1, 1), (2, 2)\}$]. Solid lines correspond to the TMSV case.

For mode b, the APN $\overline{N}_b$ is the same as $\overline{N}_a$ for the cases of both $m = n$ and $m \neq n$, i.e., $\overline{N}_a = \overline{N}_b = N$, which can be easily seen from Eq. (6).

Figure 2 shows the total APN ($2N$) before injecting into the MZI as the function of the squeezing parameter z for different superposition parameters $s = 0, 0.5, 1$. For a comparison, the APN of the TMSV is also plotted in Fig. 2; see the solid black line. From Fig. 2, it is clear that the APN of the generated states outperforms that of the TMSV in nearly all squeezing ranges for both single-side and two-side GSP operations. In addition, for a fixed superposition s, the APN increases as the increasing (m, n) and z. The APN with two-side symmetrical GSP [$(m, n) \in \{(1, 1), (2, 2)\}$] is bigger than that with single-side GSP [$(m, n) \in \{(1, 0), (2, 0)\}$], as seen by comparing Fig. 2(a) with Fig. 2(b). On the other hand, it is interesting to notice that, for fixed m and n, the APN decreases as the increasing s. In particular, in the limit $s = 0$, corresponding to the PS-then-PA case, the APN has the biggest value when other parameters are fixed. While for the case of $s = 1$ corresponding to the PA-then-PS case, the APN has the lowest value when comparing with other cases for s. Even so, both PA-then-PS and PS-then-PA have bigger APN than the TMSV. Among these non-Gaussian operations, the PS-then-PA case presents the biggest APN.

In Fig. 3, under the same parameter of $m = n = 1$, we also compare the APN $2N$ changing with z for giving several non-Gaussian states, including the PA-TMSV (magenta dashed), the PS-TMSV (cyan dashed), and the GSP-TMSV. The APN of the GSP-TMSV is always greater than that of the PS-TMSV

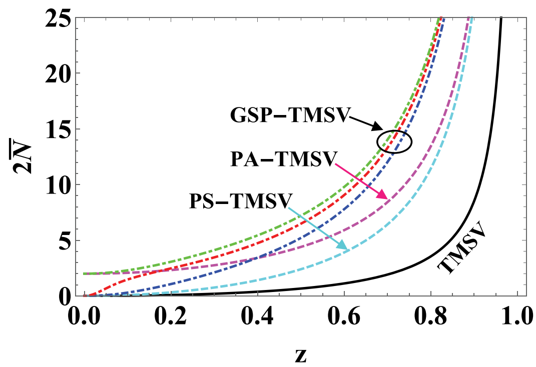

FIG. 3. As a comparison, the APN as a function of the squeezing parameter z. The dot-dashed lines represent our scheme for operation parameters $s = 0, 0.5, 1$ (corresponding to green, red, and blue lines, respectively), and dashed lines represent the previous work of using the PA-TMSV (magenta line) and the PS-TMSV (cyan line) as inputs. Solid line corresponds to the TMSV case.

for all squeezing ranges. Especially for the PS-then-PA TMSV ($s = 0$), its APN has the best performance compared to the other cases for PA-TMSV and PS-TMSV. This means that our scheme can show the advantage of the total APN, which is beneficial for the improvement of the QFI. We also notice that, compared to that of the PA-TMSV, the APN for the case of $s = 0.5$ ($s = 1$) has poor performance limited at $z < 0.18$ ($z < 0.4$), respectively.

2. Antibunching effect of the GSP-TMSV

In this subsection, let us consider the nonclassical properties of the GSP-TMSV through the antibunching effect, which reflects the sub-Poisson distribution, implying the existence of nonclassical states [46]. For an arbitrary two-mode system, generally, the criteria of the antibunching effect turns out to be [18,47]

$$R_{a,b} = \frac{\langle a^{\dagger 2}a^2\rangle + \langle b^{\dagger 2}b^2\rangle}{2\langle a^\dagger a b^\dagger b\rangle} - 1. \tag{9}$$

According to Eq. (6), we can obtain the explicit expression of antibunching effect $R_{a,b}$ in theory. In principle, the condition of $R_{a,b} < 0$ corresponds to the existence of the antibunching effect, which means that this quantum state has nonclassicality. To clearly see this point, in Fig. 4, we show the antibunching effect $R_{a,b}$ as the function of squeezing parameter z for different several superposition values $s = 0, 0.5, 1$, together with the single-side $[(m, n) \in \{(1, 0), (2, 0)\}]$ and the two-side symmetric GSP operations $[(m, n) \in \{(1, 1), (2, 2)\}]$. It is found that the GSP-TMSV states, involving the single-side GSP case [see Fig. 4(a)] and the two-side symmetric GSP cases [see Fig. 4(b)] always present the antibunching effect, which indicates the usage of the GSP operations make it possible to show the nonclassicality. However, this criteria of the antibunching effect cannot reflect how the change of $s = 0, 0.5, 1$ in our scheme affects the strength of the nonclassicality.

3. Two-mode squeezing property

To solve the aforementioned problem, in this subsection, we further discusses the two-mode squeezing property of

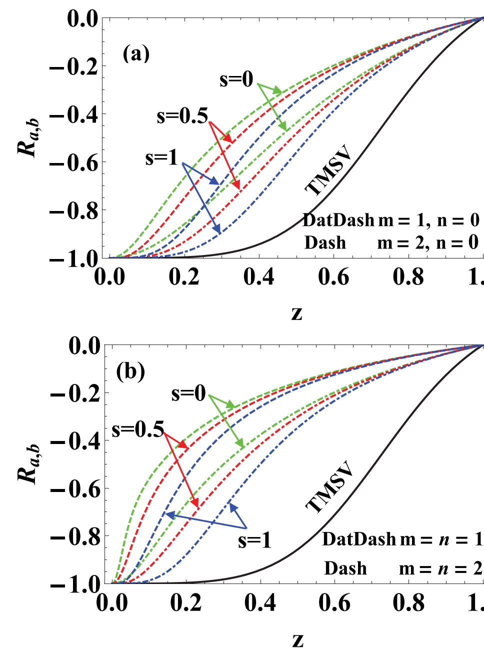

FIG. 4. The antibunching effect $R_{a,b}$ as a function of squeezing parameter z for different operator parameter $s = 0, 0.5, 1$ for (a) the single-side GSP operations $[(m, n) \in \{(1, 0), (2, 0)\}]$ and (b) the two-side symmetric GSP operations $[(m, n) \in \{(1, 1), (2, 2)\}]$. Solid lines correspond to the TMSV case.

the GSP-TMSV state by using $\langle \Delta X_1^2\rangle$ and $\langle \Delta X_2^2\rangle$, where $\langle \Delta X_i^2\rangle = \langle X_i^2\rangle - \langle X_i\rangle^2$ $(i = 1, 2)$ and X_1 (X_2) are the sum (difference) of the orthogonal components of X_a and X_b, i.e., $X_1 = X_a + X_b$ $(X_2 = X_a - X_b)$ with $X_a = (ae^{-i\theta_1} + a^\dagger e^{i\theta_1})/\sqrt{2}$ and $X_b = (be^{-i\theta_2} + b^\dagger e^{i\theta_2})/\sqrt{2}$. For a given two-mode system, its two-mode variances are given by [48]

$$\langle \Delta X_{1,2}^2\rangle = 1 + 2\langle a^\dagger a\rangle \pm 2\langle ab\rangle \cos(\theta_1 + \theta_2). \tag{10}$$

For simplicity, here we take $\theta_1 + \theta_2 = \pi$. From Eqs. (6) and (10), when $m = n = 0$, we can obtain $\langle \Delta X_1^2\rangle = (1 - z)/(1 + z)$ and $\langle \Delta X_2^2\rangle = (1 + z)/(1 - z)$, which are compatible with the TMSV case, as expected. Note that for the two-mode vacuum state $|00\rangle$, $\langle \Delta X_1^2\rangle|_{|00\rangle} = \langle \Delta X_2^2\rangle|_{|00\rangle} = 1$, which is a standard noise. Therefore, by using a logarithmic scale defined as $\text{dB}[X_1|_{|\psi\rangle}] = 10\log_{10}[\langle \Delta X_1^2\rangle|_{|\psi\rangle}/\langle \Delta X_1^2\rangle|_{|00\rangle}]$ and $\text{dB}[X_2|_{|\psi\rangle}] = 10\log_{10}[\langle \Delta X_2^2\rangle|_{|\psi\rangle}/\langle \Delta X_2^2\rangle|_{|00\rangle}]$, one can quantify the two-mode squeezing property of an arbitrary two-mode quantum state $|\psi\rangle$. If $\text{dB}[X_1|_{|\psi\rangle}] < 0$ or $\text{dB}[X_2|_{|\psi\rangle}] < 0$, in general, the state $|\psi\rangle$ can be viewed as a squeezed state.

To study the improvement of two-mode squeezing property between the GSP-TMSV and the initial TMSV, in Fig. 5, we plot the difference $\Delta\text{dB}[X_1] = 10\log_{10}[\langle \Delta X_1^2\rangle|_{|\psi\rangle_{ab}}/\langle \Delta X_1^2\rangle|_{\text{TMSV}}]$ as the function of z with several superposition values $s = 0, 0.5, 1$, including the single-side GSP operations $[(m, n) \in \{(1, 0), (2, 0)\}]$ and the two-side symmetric GSP operations $[(m, n) \in \{(1, 1), (2, 2)\}]$. In principle, the condition of $\Delta\text{dB}[X_1] < 0$ means the existence and improvement of two-mode squeezing property, but $\Delta\text{dB}[X_1] \geqslant 0$ only indicates that two-mode squeezing property cannot be enhanced. It is interesting that, as for the two types of the GSP operations, the improved area

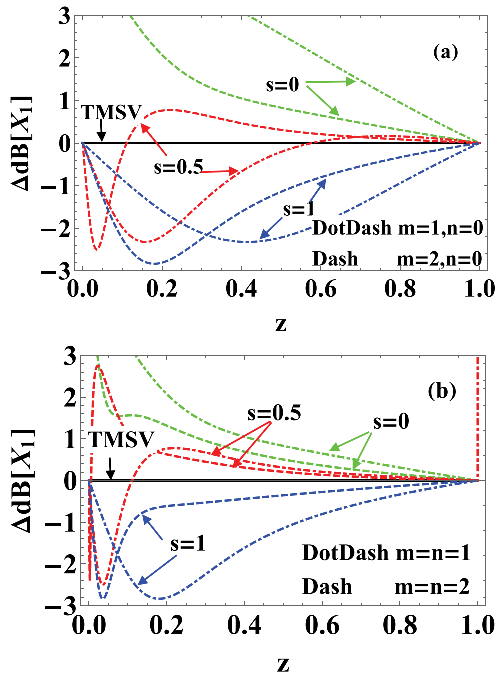

FIG. 5. The two-mode squeezing property $\Delta \mathrm{dB}[X_1|_{|\psi\rangle}]$ as a function of squeezing parameter z for different operator parameter $s = 0, 0.5, 1$ for (a) the single-side GSP operations $[(m, n) \in \{(1, 0), (2, 0)\}]$ and (b) the two-side symmetric GSP operations $[(m, n) \in \{(1, 1), (2, 2)\}]$. Solid lines correspond to the TMSV case.

of two-mode squeezing property for $s = 0$ cannot be shown, which means that using PS-then-PA operation on the TMSV makes it impossible to present the improvement of two-mode squeezing property. Whereas for other cases for $s = 0.5$ and 1, the latter can always show the existence and improvement of two-mode squeezing property, and the improved area of two-mode squeezing property for the former would be limited at a small squeezing range. Besides, with the increase of (m, n), this limitation is more obvious with respect to the narrower of achievable squeezing ranges. We also notice that, at a fixed s, for the case of $s = 0.5$, the achievable squeezing range for the single-side GSP operations are bigger than that for the two-side symmetric GSP operations in terms of the improvement of the two-mode squeezing property.

III. IMPROVEMENT OF THE QFI VIA THE GSP-TMSV

After evaluating the nonclassical properties of the GSP-TMSV, then we consider whether the GSP-TMSV can be used to improve the QFI when the GSP-TMSV is used as inputs of the balanced MZI, which consists of two symmetrical beam splitters (BSs), shown in Fig. 1 (box 2). In Ref. [49], it is pointed out that the behavior of a BS can be described as a rotation, i.e., using the Schwinger representation of SU(2) algebra,

$$J_1 = \frac{1}{2}(a^\dagger b + ab^\dagger), \quad J_2 = \frac{1}{2i}(a^\dagger b - ab^\dagger),$$
$$J_3 = \frac{1}{2}(a^\dagger a - b^\dagger b), \quad J_0 = \frac{1}{2}(a^\dagger a + b^\dagger b), \tag{11}$$

where J_0 is a Casimir operator that commutes with all others angular momentum operators $[J_i, J_0] = 0$ $(i = 1, 2, 3)$, which should satisfy the commutation relation $[J_i, J_j] = i\varepsilon_{ijk}J_k$ $(i, j, k = 1, 2, 3)$, and then the action of the MZI can be equivalent to the following unitary operator

$$U(\varphi) = e^{i\pi J_1/2}e^{-i\varphi J_3}e^{-i\pi J_1/2} = e^{-i\varphi J_2}. \tag{12}$$

Thus, when inputting any pure state $|\mathrm{in}\rangle$ into the MZI, the output state is given by

$$|\mathrm{out}\rangle_{\mathrm{MZI}} = e^{-i\varphi J_2}|\mathrm{in}\rangle. \tag{13}$$

Combining Eqs. (2) and (13), for our scheme, the resulting state prior to the parity detection can be derived as

$$|\mathrm{out}\rangle_{\mathrm{MZI}} = \frac{\mathrm{Re}\, u}{\sqrt{P_d}} e^{a^\dagger b^\dagger v\cos\varphi + \frac{1}{2}(b^{\dagger 2} - a^{\dagger 2})v \sin\varphi}|00\rangle, \tag{14}$$

where we have used $e^{i\varphi J_2}|00\rangle = |00\rangle$ and the following transformation relations,

$$e^{-i\varphi J_2}a^\dagger e^{i\varphi J_2} = a^\dagger \cos\frac{\varphi}{2} + b^\dagger \sin\frac{\varphi}{2},$$
$$e^{-i\varphi J_2}b^\dagger e^{i\varphi J_2} = b^\dagger \cos\frac{\varphi}{2} - a^\dagger \sin\frac{\varphi}{2}. \tag{15}$$

In particular, for the case of $m = n = 0$, Eq. (14) reduces to

$$|\mathrm{TMSV}\rangle = \sqrt{1 - z^2}e^{z[a^\dagger b^\dagger \cos\varphi + \frac{1}{2}(b^{\dagger 2} - a^{\dagger 2})\sin\varphi]}|00\rangle, \tag{16}$$

which is just the result in Ref. [8], where the TMSV is used as inputs of the MZI, and the superresolution and sub-Heisenberg sensitivity can be achieved using parity detection. It is interesting that, due to the fact that the usefulness of non-Gaussian (PA- and PS-) operations for achieving the strongly nonclassical states, the PS-(PA-)based TMSV scheme has been proposed for further improving the measurement precision of quantum metrology. Then a question naturally arises: Can our proposed GSP-TMSV scheme improve the phase sensitivity and resolution in quantum metrology?

Next, we first consider the proposed GSP-TMSV as the input of the MZI to study its QFI denoted by F_Q. The QFI is associated with the ultimate limit of phase sensitivity, which is given by the quantum Cramer-Rao boundary (QCRB) [50], i.e.,

$$\Delta\phi_{\min} = \frac{1}{\sqrt{F_Q}}. \tag{17}$$

In particular, for any pure state $|\psi(\theta)\rangle$, the QFI can be calculated as

$$F_Q = 4\{\langle\psi'(\theta)|\psi'(\theta)\rangle - |\langle\psi'(\theta)|\psi(\theta)\rangle|^2\}, \tag{18}$$

where $|\psi(\theta)\rangle = e^{-i\theta J_3}e^{-i\pi J_1/2}|\mathrm{in}\rangle$ and $|\psi'(\theta)\rangle = \partial|\psi(\theta)\rangle/\partial\theta$. Thus, for the GSP-TMSV state shown in Eq. (2), the QFI can be directly calculated as

$$F_Q = 2\langle aa^\dagger bb^\dagger\rangle - \langle bb^\dagger\rangle - \langle aa^\dagger\rangle$$
$$- \langle b^2 a^{\dagger 2}\rangle - \langle a^2 b^{\dagger 2}\rangle, \tag{19}$$

where the expectation values can be derived using Eq. (6). Especially, for the case of $m = n = 0$ corresponding to the TMSV as inputs, Eq. (19) reduces to $F_Q = 4z^2/(1 - z^2)^2$, as expected [20].

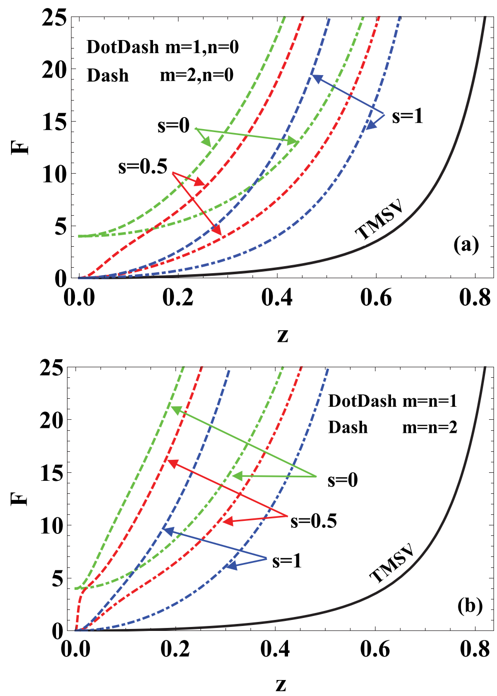

FIG. 6. Plots of the quantum Fisher information F_Q against the squeezing parameter z for different operator parameter $s = 0, 0.5, 1$ for (a) the single-side GSP operations $[(m, n) \in \{(1, 0), (2, 0)\}]$ and (b) the two-side symmetric GSP operations $[(m, n) \in \{(1, 1), (2, 2)\}]$. Solid lines correspond to the TMSV case.

According to Eq. (19), we illustrate the QFI as a function of z for the single-side $[(m, n) \in \{(1, 0), (2, 0)\}]$ and the two-side symmetric GSP operations $[(m, n) \in \{(1, 1), (2, 2)\}]$, as shown in Figs. 6(a) and 6(b), respectively. It is obvious that the QFI using TMSV input (the black solid line) is outperformed by that using the GSP-TMSV for these two cases above. Specifically speaking, when given some parameters s and z, the QFI of our scheme increases with the increase of (m, n), especially for two-side symmetric GSP operations. The reason may be the fact that the APN of the GSP-TMSV increases with the increasing (m, n) (see Fig. 2). In addition, at some fixed parameters (m, n) and z, it is found that the QFI corresponding to the PS-then-PA operation ($s = 0$) is always better than other cases, including $s = 1$ and $s = 0.5$. In addition, compared to the cases with $s = 0$ and $s = 0.5$, the QFI using PA-then-PS operation has a relatively poor improvement.

In order to highlight the advantages of the GSP-TMSV as the input of the MZI, we further make a comparison about the QFI for several different non-Gaussian states, such as single PA-TMSV (magenta dashed), single PS-TMSV (cyan dashed), and the GSP-TMSV with $m = n = 1$. The QFI as a function of squeezing parameter z is plotted in Fig. 7. It is interesting that both PA and PS operations always achieve an improvement of the QFI compared to the TMSV in the whole squeezing parameter region, while the PA operation presents a better performance than the PS operation. In addition, for the two cases with $s = 1$ and $s = 0.5$, the QFI can be also improved when the squeezing parameter exceeds a small threshold. The latter with $s = 0.5$ performs better than the former with $s = 1$. However, among these non-Gaussian

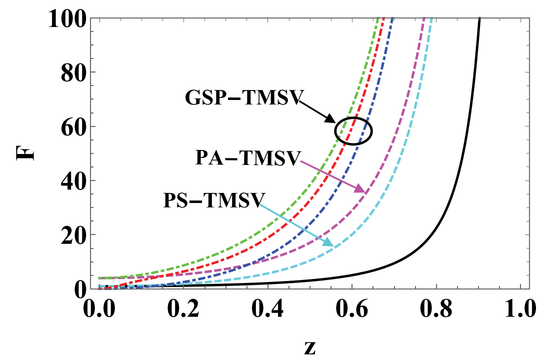

FIG. 7. As a comparison, the QFI F_Q as a function of the squeezing parameter z. The dot-dashed lines represent our scheme for operation parameter $s = 0, 0.5, 1$ (corresponding to green, red, and blue lines, respectively), and dashed lines represent the previous work of performing the PA-TMSV (magenta line) and the PS-TMSV (cyan line). Solid line corresponds to the TMSV case.

operations, the PS-then-PA operation ($s = 0$) presents the best improvement in the whole squeezing parameter region. These results are similar to the APN cases of different (non-)Gaussian states (see Fig. 3).

IV. PHASE ESTIMATION WITH PARITY DETECTION

In this section, we considered the practical precision with parity detection. Actually, the practical precision depends on the way of measure. In this section, we further examine the phase estimation using special measures. Note that the parity detection has advantages over the other detection schemes, and thus here we shall take the parity detection as a powerful tool for analyzing the phase sensitivity of our scheme.

A. The parity detection

In fact, the aim of parity detection is to obtain the expectation value of the parity operator in the output state of the MZI [51], which plays a vital role in quantum measurements. In particular, when the TMSV is used as the input, the parity detection can effectively extract the phase information, while the intensity detection is not applicable [43]. For convenience, we choose the b mode of the output, and then the parity operator can be written as

$$\Pi_b = e^{i\pi b^\dagger b} = \int \frac{d^2\gamma}{\pi} |\gamma\rangle\langle -\gamma|, \tag{20}$$

where $|\gamma\rangle$ is the coherent state, such that for an arbitrary output state $\rho_{\text{out}} = |\text{out}\rangle_{\text{MZI}}\langle \text{out}|$ in the MZI, the corresponding expectation value of Π_b can be expressed as

$$\langle \Pi_b \rangle = \mathtt{Tr}[\Pi_b \rho_{\text{out}}] = \int \frac{d^2\gamma}{\pi} \langle -\gamma | \rho_{\text{out}} | \gamma \rangle. \tag{21}$$

Thus, based on Eq. (13), the expectation value $\langle \Pi_b \rangle$ can be calculated as

$$\langle \Pi_b(\varphi) \rangle = \widetilde{\text{Re}} \frac{u u_1 \Omega_1}{P_d \sqrt{\Omega_2 - \Omega_3}}, \tag{22}$$

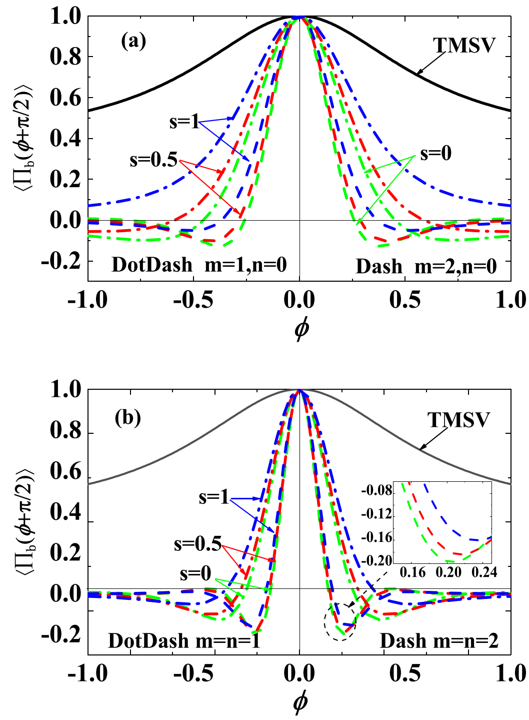

FIG. 8. The expectation values of the parity operator $\langle\Pi_b(\phi+\pi/2)\rangle$ vs the phase shift ϕ for a given squeezed parameter $z=0.6$ and different operator parameter $s=0, 0.5, 1$. (a) The single-side GSP operations $[(m,n)\in\{(1,0),(2,0)\}]$ and (b) the two-side symmetric GSP operations $[(m,n)\in\{(1,1),(2,2)\}]$. Solid lines correspond to the TMSV case.

with

$$\Omega_1=(1-v_1v\sin^2\varphi)^{\frac{1}{2}},$$
$$\Omega_2=(v_1v\cos 2\varphi+1)^2,$$
$$\Omega_3=v_1v(vv_1-1)^2\sin^2\varphi. \tag{23}$$

In particular, when $m=n=0$, Eq. (22) reduces to $\langle\Pi_b(\varphi)\rangle=(1-z^2)/\sqrt{(1-2z^2\cos 2\phi+z^4)}$ $(\varphi=\phi+\pi/2)$, corresponding to the TMSV case, as expected [8]. In the following, we will use the parameter ϕ to investigate the resolution and sensitivity.

In Ref. [8], it has been shown that the central peak of $\langle\Pi_b(\phi+\pi/2)\rangle$ at $\phi=0$ for the TMSV inputs is narrower than that for the coherent state input under the same parameters. However, it is interesting that the case can be further improved using our scheme. For given squeezing parameter $z=0.6$, using Eq. (22) we illustrate the expectation values $\langle\Pi_b(\phi+\pi/2)\rangle$ as a function of the phase shift ϕ in Fig. 8, including both the single-side GSP operations $[(m,n)\in\{(1,0),(2,0)\}$ in Fig. 8(a)] and the two-side symmetric GSP operations $[(m,n)\in\{(1,1),(2,2)\}$ in Fig. 8(b)].

From Fig. 8, it is clear that the central peak of $\langle\Pi_b(\phi+\pi/2)\rangle$ at $\phi=0$ for all the GPS-TMSV inputs is much narrower than that for the TMSV input. It implies that the use of the GSP operation is beneficial for significantly increasing the phase sensitivity. Among these non-Gaussian operations, the PS-then-PA operation $(s=0)$ presents the best performance again. In addition, for both the single-side [Fig. 8(a)] and two-side [Fig. 8(b)] GSP operations, the resolution can be further enhanced by increasing the parameter (m,n). Compared to the single-side case, the two-side case has a better performance for the improvement of resolution under the same parameters.

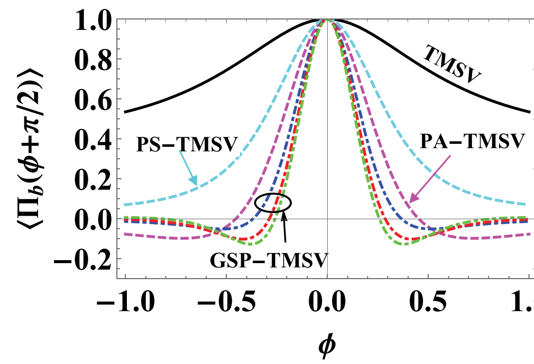

FIG. 9. The expectation values of the parity operator $\langle\Pi_b(\phi+\pi/2)\rangle$ as a function of ϕ for fixed squeezed parameter $z=0.6$ for different non-Gaussian operations. The dot-dashed lines represent the our work for operation parameter $s=0, 0.5, 1$ (green, red, and blue lines, respectively), and dashed lines represent the previous work performing the PA (magenta line) and the PS operations (cyan line). Solid line corresponds to the TMSV case.

In Fig. 9, we make a comparison about $\langle\Pi_b(\phi+\pi/2)\rangle$ between single PA(PS)-TMSVs and our proposed scheme with $m=n=1$ for a given squeezing parameter $z=0.6$. It is obvious that these non-Gaussian operations can effectively enhance the resolution and the effects of improvement can be ranked from small to large, i.e., PS, PA, PA-then-PS $(s=1)$, PA-then-PS plus PS-then-PA $(s=0.5)$, and PS-then-PA $(s=0)$. Thus, compared to both PA and PS, our scheme presents the advantages for further improving resolution, especially for PS-then-PA $(s=0)$.

B. The phase sensitivity

After investigating the resolution of our scheme in the MZI, in this subsection, we further consider the sensitivity of phase estimation based on the outcome of parity detection. In general, the phase sensitivity of the MZI can be estimated by the error propagation formula [52,53], i.e.,

$$\Delta\phi=\frac{\sqrt{1-\langle\Pi_b(\varphi)\rangle^2}}{|\partial\Pi_b/\partial\phi|}. \tag{24}$$

In particular, when $m=n=0$, corresponding to the case of TMSV input, using Eq. (22) then Eq. (24) reduces to $\Delta\phi_{\mathrm{TMSV}}=(1-2z^2\cos 2\phi+z^4)/\{[2z(1-z^2)\cos\phi]\}$, as expected. In the limit of $\phi\to 0$, $\Delta\phi_{\mathrm{TMSV}}$ becomes $\Delta\phi_{\min}=(1-z^2)/(2z)=1/\sqrt{F_Q}$, in which F_Q is the QFI for the TMSV input into the MZI. This indicates that the QCRB can be achieved especially at $\phi\to 0$ with the help of the parity detection.

Generally, lower values of $\Delta\phi$ correspond to higher phase sensitivity. In order to clearly see the effects of different parameters on the phase sensitivity, at fixed values of $z=0.6$ and $s=0, 0.5, 1$, we plot the phase sensitivity $\Delta\phi$ as a function of the phase ϕ for the single-side $[(m,n)\in\{(1,0),(2,0)\}]$ and the two-side $[(m,n)\in\{(1,1),(2,2)\}]$ symmetric GSP operations in Figs. 10(a) and 10(b),

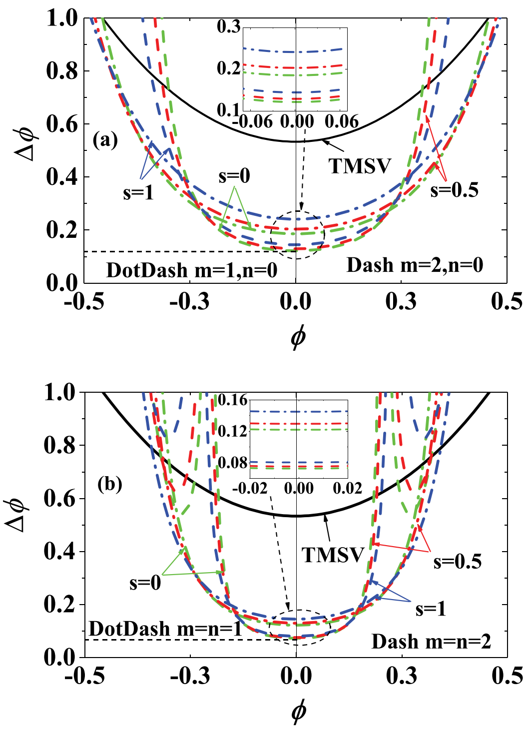

FIG. 10. The phase uncertainty $\Delta\phi$ vs the phase shift ϕ for a given squeezed parameter $z = 0.6$ and different operator parameter $s = 0, 0.5, 1$. (a) The single-side GSP operations $[(m, n) \in \{(1, 0), (2, 0)\}]$, and (b) the two-side symmetric GSP operations $[(m, n) \in \{(1, 1), (2, 2)\}]$. Solid lines correspond to the TMSV case.

respectively. Compared to the TMSV case, the minimum value of $\Delta\phi_{\min}$ can be significantly reduced by single- and two-side cases above. For given parameter s, the $\Delta\phi_{\min}$ can be further decreased with the increasing of the parameters (m, n). Comparing the single-side case with the two-side case [Figs. 10(a) and 10(b)], it is clear that the latter can achieve a lower $\Delta\phi_{\min}$ than the former. In addition, the PS-then-PA $(s = 0)$ is the best operation for getting the minimum value $\Delta\phi$ under the condition that other parameters are the same.

In Fig. 11, we further make a comparison about $\Delta\phi_{\min}$ between single PA(PS)-TMSVs and our proposed scheme, where the condition is the same as that in Fig. 10. In terms of minima $\Delta\phi_{\min}$, the effects for these non-Gaussian operations can be ranked from large to small, i.e., PS, PA, PA-then-PS $(s = 1)$, PA-then-PS plus PS-then-PA $(s = 0.5)$, and PS-then-PA $(s = 0)$. Again, the PS-then-PA is the best choice for achieving the minima of $\Delta\phi_{\min}$ due to the fact that the APN can be increased by the PS-then-PA. These results indicate that under the same parameters the phase sensitivity $\Delta\phi$ can be further enhanced by using our scheme when comparing to the PA-TMSV and the PS-TMSV.

On the other hand, it is interesting to notice that the HL based on parity detection can be beaten when the TMSV is considered as the input of the MZI [8]. However, when the PA-TMSV or PS-TMSV is used as input, the HL cannot be beaten and the corresponding phase uncertainties perform worse compared to the TMSV under the same parameters [20]. Then how about our scheme? In order to clearly see this point, for given phase $\phi = 0.05$ and $s = 0, 0.5, 1$, we show the

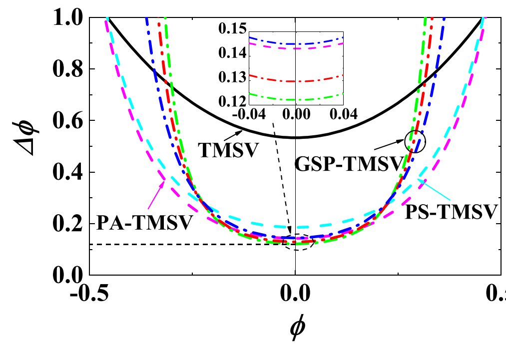

FIG. 11. As a comparison, the phase uncertainty $\Delta\phi$ as a function of the phase shift ϕ for fixed squeezed parameter $z = 0.6$. The dot-dashed lines represent the our work for operation parameter $s = 0, 0.5, 1$ (corresponding to green, red, and blue lines, respectively), and dashed lines represent the previous work of performing the PA-TMSV (magenta line) and the PS-TMSV (cyan line). Solid line corresponds to the TMSV case.

phase sensitivity as function of the total APN $2N$ for single-side $[(m, n) \in (1, 0)]$ and two-side symmetric GSP operations $[(m, n) \in (1, 1)]$ in Figs. 12(a) and 12(b), respectively. For our scheme, it is shown that the SQL is always broken through due to the fact that the GSP-TMSV is a kind of nonclassical state. As discussed above, the PS-then-PA $(s = 0)$ can be used to achieve the best phase sensitivity; however, the phase sensitivity is not below the HL for this case, but by the cases of $s = 0.5, 1$ in the regime of the small total APN (or, say, the small initial squeezing parameter z). The reason may be that, except for $s = 0$, the two-mode squeezing property can

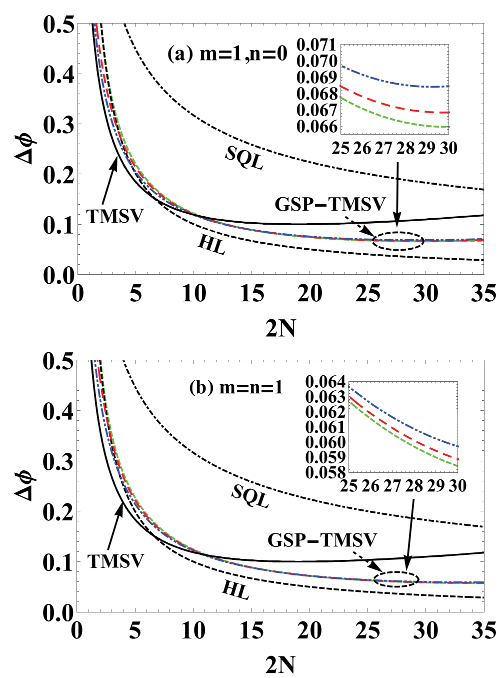

FIG. 12. The phase sensitivity $\Delta\phi$ as a function of the total APN $2N$ for different operator parameter $s = 0, 0.5, 1$ for (a) the single-side GSP operations $[(m, n) \in (1, 0)]$ and (b) the two-side symmetric GSP operations $[(m, n) \in (1, 1)]$. Solid lines correspond to the TMSV case.

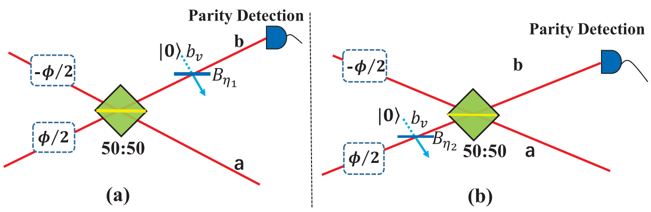

FIG. 13. Schematic diagram of the photon losses (a) in front of the parity detection (denoted as an external loss) and (b) between the phase shifter and the second BS (denoted as an internal loss).

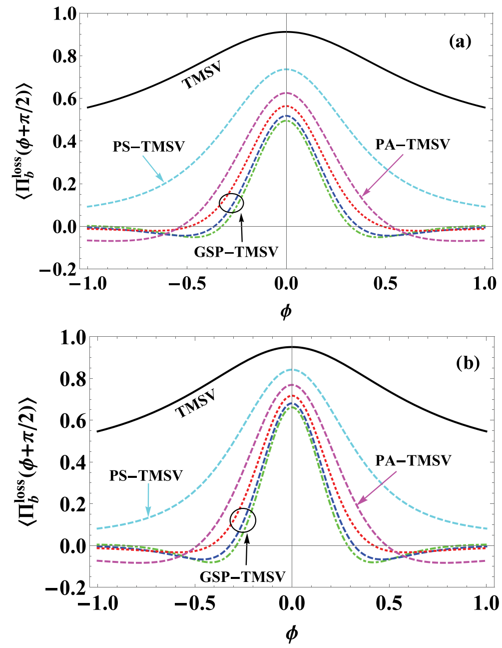

FIG. 14. The expectation values of the parity operator $\langle \Pi_b(\phi+\pi/2)\rangle$ with (a) external losses and (b) internal losses as a function of ϕ for some fixed parameter $z=0.6$, $\eta_1=\eta_2=0.9$, and $m=n=1$. The dot-dashed lines represent the our work for several different $s=0, 0.5, 1$ (corresponding to green, red, and blue dot-dashed line, respectively). As a comparison, dashed lines represent the previous work performing the PA (magenta line) and the PS operations (cyan line). Solid line corresponds to the TMSV case.

be always improved for the cases of $s=0.5, 1$ at the certain range of z, which can be seen from Fig. 5. In addition, it is also interesting to notice that comparing with single-side GSP operation $(m,n)\in(1,0)$, two-side GSP operation $(m,n)\in(1,1)$ is much easier to make the phase uncertainty close to the HL in the larger total APN region. In particular, the phase uncertainty associated with the state of our scheme is closer to the corresponding HL than the TMSV in the larger total APN region. From the above analysis, we can see that, with the same average photon number, the GSP-TMSV performs better than that of the TMSV when the average photon number is relatively large, while it is opposite when the average photon number is small. Therefore, we should mention that the GSP operation can increase the QFI of phase measurement compared with the input TMSV state. It does not mean that the GSP-TMSV state can outperform the TMSV state with the same average photon number.

V. EFFECTS OF PHOTON LOSSES ON PHASE SENSITIVITY

In practice, the traveling states are inevitably coupled to the environment, so that the decoherence process should be taken into account. Generally, there are several models of decoherence processes, such as photon loss, phase diffusion, and thermal noise. As described in Ref. [54], particularly, it is shown that the photon losses have a significant impact on phase sensitivity. Thus, here we only consider the effects of photon loss for $(m,n)=(1,1)$ in our scheme, including external and internal losses shown in Figs. 13(a) and 13(b), respectively. On the other hand, in order to further study the effects of the photon losses on the QFI, we also consider the photon losses placed before and after the linear phase shift (whose schematic diagram is shown Fig. 19). For these reasons, in the following simulations, we shall give more detailed analysis for our scheme about the effects of photon losses on the phase sensitivity and the QFI. The detail calculations are shown in Appendixes B and C.

In Fig. 14, at a fixed dissipation value $\eta_1=\eta_2=0.9$, we show the expectation values $\langle\Pi_b^{\rm loss}(\phi+\pi/2)\rangle$ with the external and internal losses as a function of the phase shift ϕ for several different parameters $s=0, 0.5, 1$. It is clear that the photon-loss processes make the central peak of $\langle\Pi_b^{\rm loss}(\phi+\pi/2)\rangle$ at $\phi=0$ lower than that of $\langle\Pi_b(\phi+\pi/2)\rangle$ for the ideal cases (see Fig. 9). Nevertheless, we can see that the central peaks of $\langle\Pi_b^{\rm loss}(\phi+\pi/2)\rangle$ at $\phi=0$ for all the GPS-TMSV inputs are much narrower than that for both the TMSV and the single PA(PS)-TMSVs inputs, which reveals that the GPS operations, especially for PS-then-PA ($s=0$), may help to improve the phase sensitivity even in the presence of photon losses, compared to both PA and PS. Besides, in contrast to the external-loss cases, the central peaks of $\langle\Pi_b^{\rm loss}(\phi+\pi/2)\rangle$ for the internal losses at $\phi=0$ are relatively narrower, which implies that the external losses have a greater influence on the phase sensitivity than the internal ones.

To visually display the effects of photon losses on phase sensitivity, we illustrate the phase sensitivity $\Delta\phi_L$ as a function of the phase ϕ for several dissipation values $\eta_l=1, 0.9, 0.8$ $(l=1,2)$, as shown in Fig. 15. The solid lines represent the ideal case with $\eta_l=1$ where the optimal phase point is at $\phi_{\rm opt}=0$. However, in the presence of photon losses, the optimal phase point that tends to be far away from zero for $\eta_l=$ 0.9, 0.8 is at $\phi_{\rm opt}\neq 0$, which leads to the decrease of phase sensitivity. The reason may be that the noise could be suppressed in near decorrelation point ($\phi=0$), as shown in Ref. [55]. Furthermore, under the same accessible parameters except for $\eta_l=1$, the phase sensitivity $\Delta\phi_L$ for the internal losses performs better than that for the external-loss cases, which indicates that the latter has a greater impact on the precision of phase measurement. In order to show the advantages of our scheme, on the other hand, we take a fixed $\eta_l=0.9$ and make a comparison about $\Delta\phi_L$ changing with the phase ϕ for several non-Gaussian resources inputs involving single PA(PS)-TMSVs and GSP-TMSV, as shown in Fig. 16. It is found that, compared with the TMSV input (black solid line), these non-Gaussian resources can still be used for

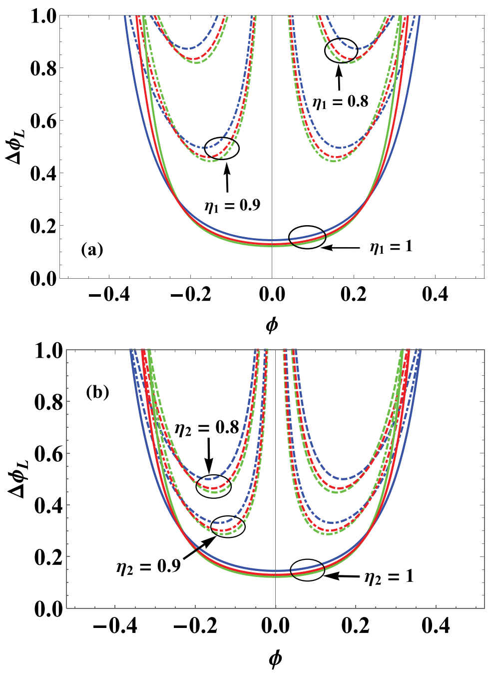

FIG. 15. The phase sensitivity with (a) external losses and (b) internal losses $\Delta\phi_L$ as a function of ϕ at some fixed parameter $z = 0.6$ and $m = n = 1$ for several dissipation values $\eta_1 = \eta_2 = 1, 0.9, 0.8$ and $s = 0, 0.5, 1$ (corresponding to green, red, and blue dot-dashed lines, respectively). As a comparison, the solid line corresponds to the ideal cases, and the dot-dashed and dashed lines represent $\eta_1 = \eta_2 = 0.9$ and $\eta_1 = \eta_2 = 0.8$, respectively.

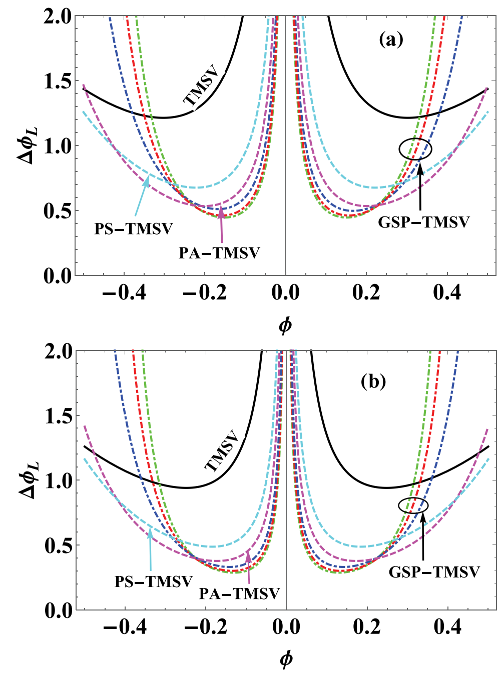

FIG. 16. The phase sensitivity $\Delta\phi_L$ with (a) external losses and (b) internal losses as a function of ϕ for some fixed parameters $z = 0.6$, $m = n = 1$, and $\eta_1 = \eta_2 = 0.9$. The dot-dashed lines represent the our work for several different $s = 0, 0.5$, and 1 (corresponding to green, red, and blue dot-dashed lines, respectively). As a comparison, dashed lines represent the previous work performing the PA (magenta line) and PS operations (cyan line). Black solid line corresponds to the TMSV case.

enhancing the phases sensitivity even in the presence of photon losses. Among them, all the GSP-TMSV inputs present better advantages for further improving the phase sensitivity when considering photon losses, in which the PS-then-PA ($s = 0$) is the best. In Fig. 17, we plot the phase sensitivity $\Delta\phi_L$ as a function of η_1(or η_2) for several non-Gaussian resources inputs mentioned above at fixed parameters $z = 0.6$ and $\phi = 0.05$, from which the phase sensitivity can be deteriorated severely with the decrease of η_1(or η_2). In contrast to the TMSV input, fortunately, the phase sensitivity can be still improved even in the presence of photon losses by using these non-Gaussian resources, especially for the GSP-TMSV. In this sense, this means that the GSP operations are more effective to resist photon losses comparing with the PA(PS) operation. In addition, the effects of the external losses on phase sensitivity are more serious than the internal-loss cases, particularly in the small η_1(or η_2) regimes.

On the other hand, as shown in Fig. 12, without losses, it is shown that the SQL can be broken for all the GSP-TMSV inputs and the phase sensitivity of our schemes are closer to the HL limit for larger values of $2N$ compared with the TMSV. In the context of photon losses, then, can the two limits be broken by using the GSP-TMSV? To this end, for some given parameters $(m, n) = (1, 1)$, $z = 0.6$, and $\phi = 0.05$, in Figs. 18(a) and 18(b), we plot the phase sensitivity $\Delta\phi_L$ as a function of total APN $2N$ for several dissipation values $\eta_l = 1, 0.99, 0.98, 0.97, 0.96$, and 0.95. It is clearly seen that the phase sensitivity decreases rapidly with the decrease of η_1(or η_2). In particular, when $\eta_1 = 0.95$, the SQL cannot be achieved for the external-loss cases but can be still broken through at large range of the total APN for the internal-loss ones. As a comparison, in Figs. 18(c) and 18(d), we repeat these graphs for TMSV, and we can find that the phase sensitivity deteriorates more quickly than our scheme with the decrease of η_1(or η_2), especially in a large range of APN $2N$. These results indicate that the external losses made against the effective improvement of phase sensitivity compared to the internal-loss cases and the effect of photon losses (including external and internal losses) on phase sensitivity can be restrained by using GSP operation.

According to Ref. [60], the effects of photon losses on the QFI cannot be ignored in practice, so here we give the schematic of a balanced MZI for the photon losses placed before and after the linear phase shifter on mode b, as shown in Fig. 19. Note that, based on Eq. (18), the photon loss after the phase shifter has no effect on the QFI. Therefore, following the approach in Ref. [61], we also assume that the photon loss occurs before and after the linear phase shifter (see Appendix B for detailed the photon-loss structure, not shown here). For a given parameter $(m, n) = (1, 1)$, Fig. 20(a) illustrates the QFI with a dissipation factor $\eta_3 = 0.9$ as a function of the squeezing parameter z with several different $s = 0, 0.5, 1$. To make a comparison, the QFI of the TMSV (black lines) with and without photon losses is also plotted. We can see that for a given dissipative value $\eta_3 = 0.9$ (dashed lines), the corresponding QFI of all the given states increases with the increase of z. Among them, the QFI of $s = 0$ has

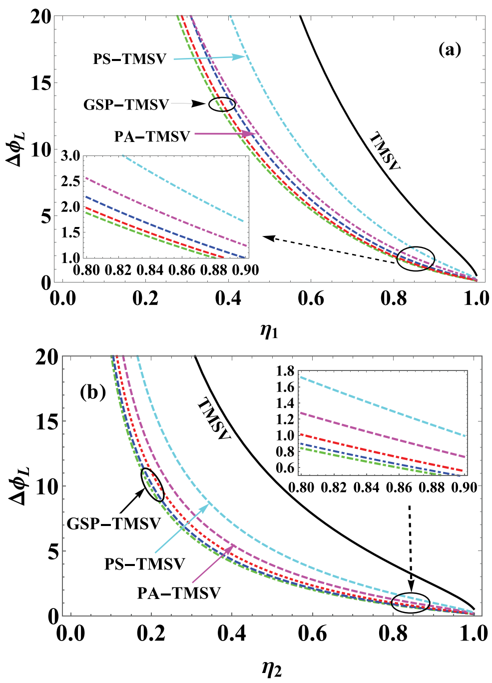

FIG. 17. The phase sensitivity with (a) external losses and (b) internal losses as a function of transmissivity of fictitious beam splitter η_1(or η_2) for some fixed parameters $z = 0.6$, $\phi = 0.05$, and $s = 0, 0.5, 1$ (green, red, and blue dot-dashed lines, respectively). As a comparison, a black solid line corresponds to the TMSV case. Cyan and purple dashed lines correspond to the PS-TMSV and the PA-TMSV, respectively.

the best performance. In addition, we also find that the gap between the QFI for the GSP-TMSV with and without photon losses is slightly larger than that of the QFI for the TMSV, which means that the GSP-TMSV as the input of optical interferometers is more sensitive to the photon losses. Even so, the QFI of the GSP-TMSV with photon losses performs better than that of the TMSV without photon losses. To further understand the QFI of the GSP-TMSV under the photon losses, at fixed $z = 0.6$ and $(m, n) = (1, 1)$, we also plot the QFI as a function of η_3 with several different $s = 0, 0.5, 1$, as shown in Fig. 20(b). We can find that, with the increase of η_3, the QFI of the GSP-TMSV, especially for $s = 0$, is enhanced significantly compared to the TMSV case. More dramatically, even in the case of severe photon losses (e.g., $\eta_3 = 0.9$), the QFI of the GSP-TMSV is still larger than that of the TMSV, which reveals that our scheme with and without photon losses has obvious advantages in increasing the QFI.

VI. CONCLUSION

In summary, we put forward an improved scheme of the phase sensitivity and resolution using a non-Gaussian quantum state, the GSP-TMSV, as the input of the MZI via parity detection. After the nonclassicality of the proposed state is discussed with respect to the APN, the antibunching effect, and two-mode squeezing property, both the QFI and the phase resolution and sensitivity based on parity detection are investigated in detail. The numerical results show that our scheme, especially for the case of the PS-then-PA TMSV, is always superior to the original TMSV scheme in terms of the QFI and the phase resolution and sensitivity, which is caused by the fact that the total APN of the former is bigger than that of the latter.

In addition, to show the advantages of our scheme, we also make performance comparisons between the GSP-TMSV and the previous PA- (or PS-) TMSV schemes about the total APN, the QFI, and the phase resolution and sensitivity. The results indicate that these performances of the previous schemes can be surpassed by our scheme, especially by the PS-then-PA TMSV. This means that the proposed GSP operation is beneficial for improving the QFI and the phase resolution and sensitivity significantly. In addition, compared with the single-side GSP operations, the improvement of two-side symmetric ones is more remarkable under the same accessible parameters. Last but not least, the SQL is always broken through by our scheme and phase sensitivity closer to the HL than the TMSV in the larger total APN region. These results show that the GSP-TMSV is a useful resource for improving phase sensitivity remarkably beyond the classical limit.

From a realistic point of view, we further study the sensitivity of phase estimation with parity detection in the presence of photon losses, including external and internal losses. The results indicate that compared to the internal photon losses, the external ones have a greater impact on phase sensitivity when several non-Gaussian resources, involving single PA- (PS-) TMSVs and GSP-TMSV, are used as the inputs. Interestingly, under the same parameters, the phase sensitivity with all the GSP-TMSV, especially for the case of $s = 0$, in the presence of photon losses can be better than that of both the TMSV and the PA(PS)-TMSV. Besides, when considering all the GSP-TMSV as the inputs of the MZI, our scheme with and without photon losses has obvious advantages in increasing the QFI well. Especially in the presence of photon losses, it is also shown that the HL cannot be beaten, but fortunately the SQL can be broken through particularly for the large total APN. Finally, we should mention that the GSP operation is probabilistic. How to improve its success probability is an interesting topic which can be studied in the future.

ACKNOWLEDGMENTS

This work is supported by the National Natural Science Foundation of China (Grants No. 11964013 and No. 11664017) and the Training Program for Academic and Technical Leaders of Major Disciplines in Jiangxi Province (No. 20204BCJL22053), and Z.L. is supported by the Fundamental Research Funds for the Central University (Grant No. 20lgpy163) at Sun Yat-sen University.

APPENDIX A: DERIVATION OF EQS. (2) AND (6)

In this Appendix, we first derive the the explicit form of Eq. (2). By using the commutation relation $[a, a^\dagger] = 1$ and $\vartheta^m = \frac{\partial^m}{\partial\tau^m} \exp(\tau\vartheta)|_{\tau=0}$, one can rewrite Eq. (1) as

$$\hat{O} = \frac{\partial^{m+n}}{\partial\tau_1^m \partial\tau_2^n} \exp(s_1\tau_1 + s_2\tau_2) \times \exp[(s_2\tau_2 + t_2\tau_2)b^\dagger b] \times \exp[(s_1\tau_1 + t_1\tau_1)a^\dagger a]|_{\tau_1=\tau_2=0}. \tag{A1}$$

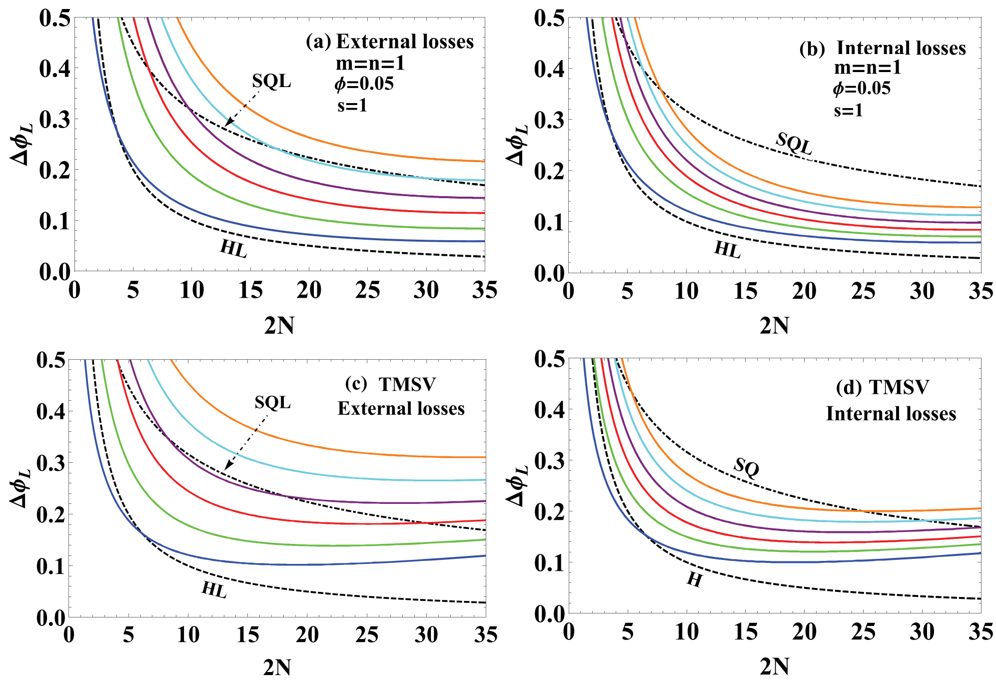

FIG. 18. The phase sensitivity $\Delta\phi_L$ with (a) external losses and (b) internal losses as a function of the total APN $2N$ at some fixed parameters $s=1, m=n=1$, and $\phi=0.05$. (c) External losses and (d) internal losses as a function of the total APN $2N$ for TMSV. The dot-dashed and dashed line correspond to the SQL and HL, respectively. The color lines from down to up correspond to dissipation value $\eta_1=\eta_2=1, 0.99, 0.98, 0.97, 0.96$ and 0.95, respectively.

Thus, by performing the GSP operations $\hat{O}$ on the each mode of the TMSV, one can obtain

$$|\psi\rangle_{ab}=\sqrt{\frac{1-z^2}{P_d}}\frac{\partial^{m+n}}{\partial\tau_1^m\partial\tau_2^n}\exp(s_1\tau_1+s_2\tau_2)\times\exp[(s_2\tau_2+t_2\tau_2)b^\dagger b]\exp[(s_1\tau_1+t_1\tau_1)a^\dagger a]\times\exp[a^\dagger b^\dagger z]|00\rangle|_{\tau_1=\tau_2=0}. \tag{A2}$$

Finally, Eq. (2) can be obtained via the relation $e^{\lambda a^\dagger a}a^\dagger e^{-\lambda a^\dagger a}=a^\dagger e^\lambda$.

Next, for the GSP-TMSV mentioned above, let us derive the expectation value of a general quantum operators $a^l b^k a^{\dagger h} b^{\dagger g}$, which can be expressed as

$$\langle a^l b^k a^{\dagger h} b^{\dagger g}\rangle=\mathrm{Tr}[|\psi\rangle_{ab}\langle\psi|a^l b^k a^{\dagger h} b^{\dagger g}]. \tag{A3}$$

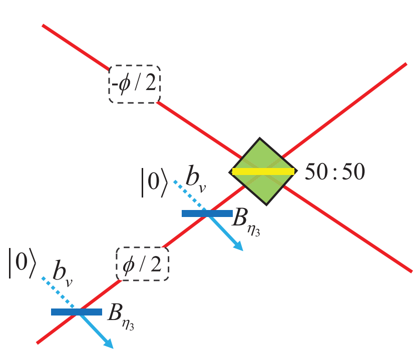

FIG. 19. Schematic diagram of a balanced MZI for the photon losses on mode B, which is placed at before and after the linear phase shifter. B_{η_3} is the BS with a transmissivity η_3 and $|0\rangle$ is the vacuum state on the auxiliary mode b_v.

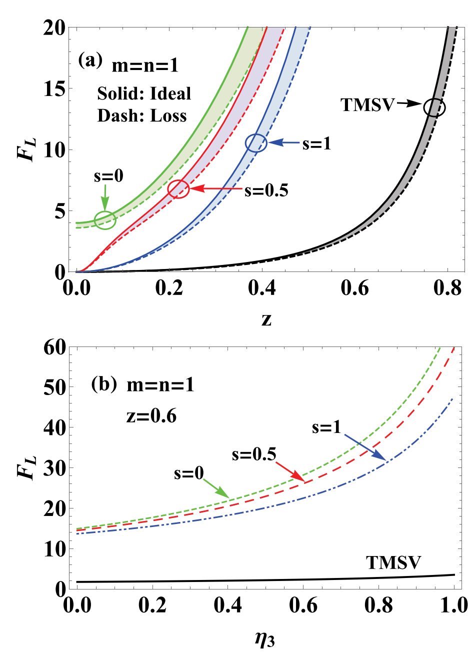

FIG. 20. The QFI in the presence of photon losses as a function of (a) squeezing parameter z with several different $s=0, 0.5, 1$ (corresponding to green, red, and blue lines) and (b) dissipation factor η_3 at fixed $z=0.6$ and $(m, n)=(1, 1)$. In panel (a), the solid and dashed lines represent $\eta_3=1$ and $\eta_3=0.9$, respectively. As a comparison, the black line corresponds to the TMSV case.

By using the completeness relation $\int d^2\alpha|\alpha\rangle\langle\alpha|/\pi = 1$ and the integral formula

$$\int \frac{d^2\gamma}{\pi} e^{\varsigma|\gamma|^2+\xi\gamma+\chi\gamma^*} = -\frac{e^{-\xi\chi/\varsigma}}{\varsigma}, (\mathrm{Re}[\varsigma] < 0), \tag{A4}$$

after doing straightforward calculation, we can obtain

$$\begin{aligned}\langle a^l b^k a^{\dagger h} b^{\dagger g}\rangle &= \mathrm{Tr}[|\psi\rangle_{ab}\langle\psi|a^l b^k a^{\dagger h} b^{\dagger g}]\\ &= \frac{\widetilde{\mathrm{Re}}\, uu_1}{P_d}\langle 00|\exp(v_1 ab)a^l b^k a^{\dagger h} b^{\dagger g}\exp(va^\dagger b^\dagger)|00\rangle\\ &= \frac{\widetilde{\mathrm{Re}}\, uu_1}{P_d}\frac{\partial^{l+k+h+g}}{\partial\tau_5^l\partial\tau_6^k\partial\tau_7^h\partial\tau_8^g}\int\frac{d^2\alpha d^2\beta}{\pi^2}\exp[-|\alpha|^2+(v_1\beta+\tau_5)\alpha+(\tau_7+v\beta^*)\alpha^*]\exp(-|\beta|^2+\tau_6\beta+\tau_8\beta^*)\\ &= \frac{\widetilde{\mathrm{Re}}\, uu_1}{P_d}\frac{\partial^{l+k+h+g}}{\partial\tau_5^l\partial\tau_6^k\partial\tau_7^h\partial\tau_8^g}\frac{1}{1-vv_1}\exp\left(\frac{\tau_7\tau_8 v_1+\tau_6\tau_5 v+\tau_6\tau_8+\tau_5\tau_7}{1-vv_1}\right)|_{\tau_5=\tau_6=\tau_7=\tau_8=0}.\end{aligned} \tag{A5}$$

which is Eq. (6).

APPENDIX B: DERIVATION OF THE PHASE SENSITIVITY WITH PARITY DETECTION IN THE PRESENCE OF PHOTON LOSSES

In order to derive the phase sensitivity with parity detection in the presence of photon losses, for simplicity, here we consider two special photon-loss processes, i.e., the external loss and the internal one, shown in Fig. 13. In practice, the photon losses on auxiliary mode b_v can be structured using a fictitious beam splitter (denoted as B_{η_i}) with a dissipation factor η_i ($i = 1$ and 2 corresponding to the external and internal losses, respectively), whose transform relation is given by [56]

$$B_{\eta_i}^\dagger\begin{pmatrix} b\\ b_v\end{pmatrix}B_{\eta_i} = \begin{pmatrix}\sqrt{\eta_i} & \sqrt{1-\eta_i}\\ -\sqrt{1-\eta_i} & \sqrt{\eta_i}\end{pmatrix}\begin{pmatrix} b\\ b_v\end{pmatrix}. \tag{B1}$$

It is worth mentioning that the smaller values of η_i correspond to the more severe photon losses. In particular, $\eta_i = 1$ corresponds to the ideal case. To get the parity operator in the presence of the external losses, on one hand, it is necessary to rewrite Eq. (20) under the Weyl ordering representation [57], i.e.,

$$\Pi_b = \frac{\pi}{2} \vdots\,\delta(b)\delta(b^\dagger)\,\vdots\,, \tag{B2}$$

where $\vdots\bullet\vdots$ denotes the symbol of the Weyl ordering and $\delta(\bullet)$ denotes the delta function. Thus, by using Eq. (B1), one can obtain the parity operator with external losses (denoted as Π_b^{loss}), namely,

$$\begin{aligned}\Pi_b^{\mathrm{loss}} = \frac{\pi}{2}\,{}_v\langle 0|\vdots\,\delta(\sqrt{\eta_i}b+\sqrt{1-\eta_i}b_v)\\ \times\,\delta(\sqrt{\eta_i}b^\dagger+\sqrt{1-\eta_i}b_v^\dagger)\,\vdots\,|0\rangle_v,\end{aligned} \tag{B3}$$

where $|0\rangle_v$ is the vacuum noise input on auxiliary mode b_v. Finally, according to the classical correspondence of the operator

$$\begin{aligned}\vdots\, f(b, b^\dagger, b_v, b_v^\dagger)\,\vdots\, = 4\int d^2\beta d^2\gamma f(\beta,\beta^*,\gamma,\gamma^*)\\ \times\,\Delta(\beta,\beta^*)\Delta(\gamma,\gamma^*),\end{aligned} \tag{B4}$$

with Wigner operators under the normal ordering [58]

$$\begin{aligned}\Delta(\beta,\beta^*) &=: \exp[-2(b^\dagger-\beta^*)(b-\beta)]:,\\ \Delta(\gamma,\gamma^*) &=: \exp[-2(b_v^\dagger-\gamma^*)(b_v-\gamma)]:,\end{aligned} \tag{B5}$$

and using the integration within an ordered product (IWOP) technique [59], it is easy to obtain

$$\Pi_b^{\mathrm{loss}} =: e^{-2\eta_1 b^\dagger b} := (1-2\eta_1)^{b^\dagger b}, \tag{B6}$$

where the symbol :: denotes the normal ordering. Thus, combining Eqs. (14) and (B6), the average value of Π_b^{loss} for the output state can be given by

$$\langle\Pi_b^{\mathrm{loss}}\rangle = \mathrm{Tr}[\rho_{\mathrm{out}}\Pi_b^{\mathrm{loss}}] = \widetilde{\mathrm{Re}}\frac{uu_1\sqrt{\vartheta_1}}{P_d\sqrt{\vartheta_2^2-\vartheta_3}}, \tag{B7}$$

with

$$\begin{aligned}\vartheta_1 &= 1 - vv_1\sin^2\varphi,\\ \vartheta_2 &= 1 - vv_1 + 2\eta_1 v_1 v\cos^2\varphi,\\ \vartheta_3 &= (1-2\eta_1)^2\sin^2\varphi v_1 v(1-vv_1)^2.\end{aligned} \tag{B8}$$

On the other hand, unlike the derivation of Eq. (B6), we rewrite the parity operator with the internal losses as

$$\begin{aligned}\widetilde{\Pi}_b^{\mathrm{loss}} &= {}_v\langle 0|B_1^\dagger U^\dagger(\varphi)B_v^\dagger B_2^\dagger e^{i\pi b^\dagger b}B_2 B_v U(\varphi)B_1|0\rangle_v\\ &=: e^{\varpi_1 a^\dagger a-\varpi_2 b^\dagger a-\varpi_2^* a^\dagger b+\varpi_3 b^\dagger b}:,\end{aligned} \tag{B9}$$

where $U(\varphi)$ is given in Eq. (12) and

$$\begin{aligned}\varpi_1 &= \sqrt{\eta_2}\cos\varphi - \frac{1+\eta_2}{2},\\ \varpi_2 &= \frac{(\eta_2+1)^2-4\eta_2\cos^2\varphi}{2(i\eta_2-i+2\sqrt{\eta_2}\sin\varphi)},\\ \varpi_3 &= -\sqrt{\eta_2}\cos\varphi - \frac{1+\eta_2}{2},\end{aligned} \tag{B10}$$

and we have used the following transformation relationships:

$$\begin{aligned}B_1^\dagger\begin{pmatrix} a\\ b\end{pmatrix}B_1 &= \frac{\sqrt{2}}{2}\begin{pmatrix}1 & i\\ i & 1\end{pmatrix}\begin{pmatrix} a\\ b\end{pmatrix},\\ B_2^\dagger\begin{pmatrix} a\\ b\end{pmatrix}B_2 &= \frac{\sqrt{2}}{2}\begin{pmatrix}1 & -i\\ -i & 1\end{pmatrix}\begin{pmatrix} a\\ b\end{pmatrix}.\end{aligned} \tag{B11}$$

Thus, for a given input GSP-TMSV, one can obtain the expectation value of $\widetilde{\Pi}_b^{\rm loss}$ for the internal losses, i.e.,

$$\langle \Pi_b^{\rm loss} \rangle = \mathtt{Tr}[|\psi\rangle_{ab}\langle\psi|\widetilde{\Pi}_b^{\rm loss}] = \frac{\widetilde{\rm Re}\, uu_1}{p_d}[(1-\omega_1)^2-\omega_2]^{-\frac{1}{2}}, \tag{B12}$$

with

$$\omega_1 = v_1 v(\varpi_1\varpi_3 - \eta_2 + |\varpi_2|^2),$$
$$\omega_2 = 4|\varpi_2|^2 v_1^2 v^2(\varpi_1\varpi_3 - \eta_2). \tag{B13}$$

Finally, using Eqs. (B7) and (B12), the phase sensitivity (denoted as $\Delta\phi_L$) in the presence of external and internal losses can be estimated by the error propagation formula

$$\Delta\phi_L = \frac{\sqrt{1-\langle \Pi_b^{\rm loss}\rangle^2}}{|\partial \Pi_b^{\rm loss}/\partial\phi|}. \tag{B14}$$

APPENDIX C: DERIVATION OF THE QFI IN THE PRESENCE OF PHOTON LOSSES

In order to derive the QFI in the presence of photon losses, here we shall use a general formalism for obtaining the the ultimate limit of precision in noisy systems, proposed by Escher [60]. They pointed out that the enlarged state of the system $|\psi\rangle_s$ and the environment $|0\rangle_e$ can be written as

$$|\Phi\rangle_{se} = \widehat{U}_{se}|\psi\rangle_s|0\rangle_e = \sum_\kappa \widehat{K}_\kappa(\varphi)|\psi\rangle_s|\kappa\rangle_e, \tag{C1}$$

where $\widehat{U}_{se}$ is the corresponding unitary operator, $|\psi\rangle_s$ is the initial state of the system, $|0\rangle_e$ is the initial state of the environment, $|\kappa\rangle_e$ is an orthogonal state of the environment, and $\widehat{K}_\kappa(\varphi)$ are Kraus operators that can be used to describe the photon losses. For the whole systems, the upper bound of the QFI Γ_Q is thus given by

$$\Gamma_Q[|\psi\rangle_s, \widehat{K}_\kappa(\varphi)] = 4[{}_s\langle\psi|\widehat{H}_1|\psi\rangle_s - |{}_s\langle\psi|\widehat{H}_2|\psi\rangle_s|^2], \tag{C2}$$

with

$$\widehat{H}_1 = \sum_\kappa \frac{d\widehat{K}_\kappa^\dagger(\varphi)}{d\varphi}\frac{d\widehat{K}_\kappa(\varphi)}{d\varphi},$$
$$\widehat{H}_2 = i\sum_\kappa \frac{d\widehat{K}_\kappa^\dagger(\varphi)}{d\varphi}\widehat{K}_\kappa(\varphi). \tag{C3}$$

According to Ref. [60], the relation between the QFI and the upper bound Γ_Q is written as

$$F_L = \min_{\{K_\kappa(\varphi)\}} \Gamma_Q[|\psi\rangle_s, \widehat{K}_\kappa(\varphi)]. \tag{C4}$$

For simplicity, here we consider the photon losses on mode b, whose schematic is given in Fig. 19. In this situation, a possible set of Kraus operators describing the photon-loss process is [60]

$$\widehat{K}_\kappa(\varphi) = \sqrt{\frac{(1-\eta_3)^\kappa}{\kappa!}} e^{-i\varphi\left(\frac{a^\dagger a - b^\dagger b}{2}+\frac{\epsilon\kappa}{2}\right)}\eta_3^{\frac{n_b}{2}} b^\kappa, \tag{C5}$$

where $\epsilon = 0$ and $\epsilon = -1$ respectively represent the photon losses before and after the phase shifter, and η_3 is the dissipation factor with $\eta_3 = 0$ and $\eta_3 = 1$ corresponding to the complete absorption and lossless cases, respectively. In addition, to obtain the minimum of Γ_Q, it is necessary for us to get the expressions of both $\widehat{H}_1$ and $\widehat{H}_2$, which can be respectively calculated according to Eqs. (C3) and (C5) as

$$\widehat{H}_1 = \tfrac{1}{4}n_a^2 + \tfrac{1}{4}[\eta_3 - \epsilon(1-\eta_3)]^2 n_b^2 + \tfrac{1}{2}(\epsilon - \epsilon\eta_3 - \eta_3)n_a n_b + \tfrac{1}{4}(1+\epsilon)^2\eta_3(1-\eta_3)n_b, \tag{C6}$$

$$\widehat{H}_2 = -\tfrac{1}{2}n_a + \tfrac{1}{2}[\eta_3 - \epsilon(1-\eta_3)]n_b, \tag{C7}$$

with the definitions of $n_a = a^\dagger a$ and $n_b = b^\dagger b$.

Therefore, by combining Eqs. (C2), (C3), (C6), and (C7), one can obtain

$$\Gamma_Q = \langle\Delta^2 n_a\rangle + (\eta_3 + \epsilon\eta_3 - \epsilon)^2\langle\Delta^2 n_b\rangle - 2(\eta_3+\epsilon\eta_3-\epsilon)(\langle n_a n_b\rangle - \langle n_a\rangle\langle n_b\rangle) + (1+\epsilon)^2\eta_3(1-\eta_3)\langle n_b\rangle, \tag{C8}$$

where $\langle\Delta^2 x\rangle = \langle x^2\rangle - \langle x\rangle^2$ and $\langle x\rangle$ are respectively the variance and average for the quantum state that the input state $|\psi\rangle_s$ goes through for the first BS. Finally, the minimum value of $\Gamma_Q[|\psi\rangle_s, \widehat{K}_\kappa(\varphi)]$ corresponding to the QFI in the presence of photon losses can be obtained when $\epsilon = -\zeta/\chi$ with

$$\chi = (1-\eta_3)\langle\Delta^2 n_b\rangle + \eta_3\langle n_b\rangle,$$
$$\zeta = -\eta_3\langle\Delta^2 n_b\rangle + \langle n_a n_b\rangle - \langle n_a\rangle\langle n_b\rangle + \eta_3\langle n_b\rangle, \tag{C9}$$

and $\langle n_a\rangle$, $\langle n_b\rangle$, $\langle n_a n_b\rangle$, $\langle n_a^2\rangle$, $\langle n_b^2\rangle$ can be calculated as

$$\langle n_a\rangle = \langle n_b\rangle = \frac{\widetilde{\rm Re}\, uu_1}{P_d}\frac{1}{(1-v_1 v)^2} - 1,$$
$$\langle n_a n_b\rangle = \frac{\widetilde{\rm Re}\, uu_1}{P_d}\frac{2v_1 v - 1}{(1-vv_1)^3} + 1,$$
$$\langle n_a^2\rangle = \langle n_b^2\rangle = \frac{\widetilde{\rm Re}\, uu_1}{P_d}\frac{4vv_1 - 1}{(1-vv_1)^3} + 1. \tag{C10}$$

[1] S. L. Braunstein and C. M. Caves, Statistical Distance and the Geometry of Quantum States, Phys. Rev. Lett. **72**, 3439 (1994).

[2] J. P. Dowling, Quantum optical metrology-the lowdown on high-N00N states, Contemp. Phys. **49**, 125 (2008).

[3] J. J . Bollinger, W. M. Itano, D. J. Wineland, and D. J. Heinzen, Optimal frequency measurements with maximally correlated states, Phys. Rev. A **54**, R4649 (1996).

[4] V. Giovannetti, S. Lloyd, and L. Maccone, Advances in quantum metrology, Nat. Photon. **5**, 222 (2011).

[5] C. M. Caves, Quantum-mechanical noise in an interferometer, Phys. Rev. D **23**, 1693 (1981).

[6] R. Carranza and C. C. Gerry, Photon-subtracted two-mode squeezed vacuum states and applications to quantum optical interferometry, J. Opt. Soc. Am. B **29**, 2581 (2012).

[7] H. Kwon, K. C. Tan, T. Volkoff, and H. Jeong, Nonclassicality as a Quantifiable Resource for Quantum Metrology, Phys. Rev. Lett. **122**, 040503 (2019).

[8] P. M. Anisimov, G. M. Raterman, A. Chiruvelli, W. N. Plick, and S. D. Huver, Quantum Metrology with Two-Mode Squeezed Vacuum: Parity Detection Beats the Heisenberg Limit, Phys. Rev. Lett. **104**, 103602 (2010).

[9] I. Afek, O. Ambar, and Y. Silberberg, High-NOON states by mixing quantum and classical light, Science **328**, 879 (2010).

[10] V. Giovannetti, S. Lloyd, and L. Maccone, Quantum-enhanced measurements: Beating the standard quantum limit, Science **306**, 1330 (2004).

[11] J. Joo, W. J. Munro, and T. P. Spiller, Quantum Metrology with Entangled Coherent States, Phys. Rev. Lett. **107**, 083601 (2011).

[12] T. Eberle, V. Hadchen, and R. Schnabel, Stable control of 10 dB two-mode squeezed vacuum states of light, Opt. Express **21**, 11546 (2013).

[13] N. Namekata, Y. Takahashi, G. Fujii, D. Fukuda, S. Kurimura, and S. Inoue, Non-Gaussian operation based on photon subtraction using a photon-number-resolving detector at a telecommunications wavelength, Nat. Photon. **4**, 655 (2010).

[14] L. Y. Hu, Z. Y. Liao, and M. S. Zubairy, Continuous-variable entanglement via multiphoton catalysis, Phys. Rev. A **95**, 012310 (2017).

[15] L. Y. Hu, M. Al-amri, Z. Y. Liao, and M. S. Zubairy, Entanglement improvement via a quantum scissor in a realistic environment, Phys. Rev. A **100**, 052322 (2019).

[16] G. S. Agarwal and K. Tara, Nonclassical properties of states generated by the excitations on a coherent state, Phys. Rev. A **43**, 492 (1991).

[17] A Zavatta, V. Parigi, and M. Bellini, Experimental nonclssicality of single-photon-added thermal light states, Phys. Rev. A **75**, 052106 (2007).

[18] L. Y. Hu and Z. M. Zhang, Statistical properties of coherent photon-added two-mode squeezed vacuum and its inseparability, J. Opt. Soc. Am. B **30**, 518 (2013).

[19] A. Zavatta, S. Viciani, and M. Bellini, Quantum-to-classical transition with single-photon-added coherent states of light, Science **306**, 660 (2004).

[20] Y. Ouyang, S. Wang, and L. J. Zhang, Quantum optical interferometry via the photon added two-mode squeezed vacuum states, J. Opt. Soc. Am. B **33**, 1373 (2016).

[21] S. Y. Lee, S. W. Ji, H. J. Kim, and H. Nha, Enhancing quantum entanglement for continuous variables by a coherent superposition of photon subtraction and addition, Phys. Rev. A **84**, 012302 (2011).

[22] S. Wang, L. L. Hou, X. F. Chen, and X. F. Xu, Continuous-variable quantum teleportation with non-Gaussian entangled states generated via multiple-photon subtraction and addition, Phys. Rev. A **91**, 063832 (2015).

[23] E. D. Lopaeva, I. R. Berchera, I. P. Degiovanni, S. Olivares, G. Brida, and M. Genovese, Experimental Realization of Quantum Illumination, Phys. Rev. Lett. **110**, 153603 (2013).

[24] S. H. Tan, B. I. Erkmen, V. Giovannetti, S. Guha, S. Lloyd, L. Maccone, S. Pirandola, and J. H. Shapiro, Quantum Illumination with Gaussian States, Phys. Rev. Lett. **101**, 253601 (2008).

[25] Y. Guo, W. Ye, H. Zhong, and Q. Liao, Continuous-variable quantum key distribution with non-Gaussian quantum catalysis, Phys. Rev. A **99**, 032327 (2019).

[26] W. Ye, H. Zhong, Q. Liao, D. Huang, L. Y. Hu, and Y. Guo, Improvement of self-referenced continuous-variable quantum key distribution with quantum photon catalysis, Opt. Express **27**, 17186 (2019).

[27] W. Ye, Y. Guo, Y. Xia, H. Zhong, H. Zhang, J. Z. Ding, and L. Y. Hu, Discrete modulation continuous-variable quantum key distribution based on quantum catalysis, Acta Phys. Sin. **69**, 060301 (2020).

[28] Y. J. Zhao, Y. C. Zhang, B. J. Xu, S. Yu, and H. Guo, Continuous-variable measurement-device-independent quantum key distribution with virtual photon subtraction, Phys. Rev. A **97**, 042328 (2018).

[29] H. X. Ma, P. Huang, D. Y. Bai, S. Y. Wang, W. S. Bao, and G. H. Zeng, Continuous-variable measurement-device independent quantum key distribution with photon subtraction, Phys. Rev. A **97**, 042329 (2018).

[30] Y. Yang and F. L. Li, Entanglement properties of non-Gaussian resources generated via photon subtraction and addition and continuous-variable quantum-teleportation improvement, Phys. Rev. A **80**, 022315 (2009).

[31] T. Opatrny, G. Kurizki, and D. G. Welsch, Improvement on teleportation of continuous variables by photon subtraction via conditional measurement, Phys. Rev. A **61**, 032302 (2000).

[32] S. Takeda, H. Benichi, T. Mizuta, N. Lee, J. Yoshikawa, and A. Furusawa, Quantum mode filtering of non-Gaussian states for teleportation-based quantum information processing, Phys. Rev. A **85**, 053824 (2012).

[33] A. Kitagawa, M. Takeoka, M. Sasaki, and A. Chefles, Entanglement evaluation of non-Gaussian states generated by photon subtraction from squeezed states, Phys. Rev. A **73**, 042310 (2006).

[34] Y. Yang and F. L. Li, Nonclassicality of photon-subtracted and photon-added-then-subtracted Gaussian states, J. Opt. Soc. Am. B **26**, 000830 (2009).

[35] M. S. Kim, H. Jeong, A. Zavatta, V. Parigi, and M. Bellini, Scheme for Proving the Bosonic Commutation Relation Using Single-Photon Interference, Phys. Rev. Lett. **101**, 260401 (2008).

[36] H. Zhang, W. Ye, Y. Xia, S. K. Chang, C. P. Wei, and L. Y. Hu, Improvement of the entanglement properties for entangled states using a superposition of number-conserving operations, Laser Phys. Lett. **16**, 085204 (2019).

[37] S. D. Himadri, C. Arpita, and G. Rupamanjari, Generating continuous variable entangled states for quantum teleportation using a superposition of number-conserving operations, J. Phys. B: At. Mol. Opt. Phys. **48**, 185502 (2015).

[38] S. Ataman, Optimal Mach-Zehnder phase sensitivity with Gaussian states, Phys. Rev. A **100**, 063821 (2019).

[39] L. L. Guo, Y. F. Yu, and Z. M. Zhang, Improving the phase sensitivity of an SU(1, 1) interferometer with photon-added squeezed vacuum light, Opt. Express **26**, 29099 (2018).
[40] X. Y. Hu, C. P. Wei, Y. F. Yu, and Z. M. Zhang, Enhanced phase sensitivity of an SU(1, 1) interferometer with displaced squeezed vacuum light, Front. Phys. **11**, 114203 (2016).
[41] D. Li, B. T. Gard, Y. Gao, C. H. Yuan, W. P. Zhang, H. Lee, and J. P. Dowling, Phase sensitivity at the Heisenberg limit in an SU(1, 1) interferometer via parity detection, Phys. Rev. A **94**, 063840 (2016).
[42] R. A. Campos, C. C. Gerry, and A. Benmoussa, Optical interferometry at the Heisenberg limit with twin Fock states and parity measurements, Phys. Rev. A **68**, 023810 (2003).
[43] T. Kim, O. Pfister, M. Holland, J. Noh, and J. Hall, Influence of decorrelation on Heisenberg-limited interferometry with quantum correlated photons, Phys. Rev. A **57**, 4004 (1998).
[44] C. C. Gerry, Heisenberg-limit interferometry with four-wave mixers operating in a nonlinear regime, Phys. Rev. A **61**, 043811 (2000).
[45] C. C. Gerry and R. A. Campos, Generation of maximally entangled photonic states with a quantum-optical Fredkin gate, Phys. Rev. A **64**, 063814 (2001).
[46] A. Joshia and S. V. Lawande, Properties of squeezed binomial states and squeezed negative binomial states, J. Mod. Opt. **38**, 2009 (1991).
[47] C. T. Lee, Many-photon anti-bunching in generalized pair coherent states, Phys. Rev. A **41**, 1569 (1990).
[48] W. Ye, K. Z. Zhang, H. L. Zhang, X. X. Xu, and L. Y. Hu, Laguerre-polynomial-weighted squeezed vacuum: Generation and its properties of entanglement, Laser Phys. Lett. **15**, 025204 (2018).
[49] B. Yurke, S. L. McCall, and J. R. Klauder, SU(2) and SU(1, 1) interferometers, Phys. Rev. A **33**, 4033 (1986).
[50] Y. M. Zhang, X. W. Li, W. Yang, and G. R. Jin, Quantum Fisher information of entangled coherent states in the presence of photon loss, Phys. Rev. A **88**, 043832 (2013).
[51] R. Birrittella, J. Mimih, and C. C. Gerry, Multiphoton quantum interference at a beam splitter and the approach to Heisenberg-limited interferometry, Phys. Rev. A **86**, 063828 (2012).
[52] P. R. Bevinglon, *Data Reduction and Error Analysis for the Physical Sciences* (McGraw-Hill, New York, 1969).
[53] K. P. Seshadreesan, S. Kim, J. P. Dowling, and H. Lee, Phase estimation at the quantum Cram-Rao bound via parity detection, Phys. Rev. A **87**, 043833 (2013).
[54] T. W. Lee, S. D. Huver, H. Lee, L. Kaplan, S. B. McCracken, C. Min, D. B. Uskov, C. F. Wildfeuer, G. Veronis, and J. P. Dowling, Optimization of quantum interferometric metrological sensors in the presence of photon loss, Phys. Rev. A **80**, 063803 (2009).
[55] D. Li, C. H. Yuan, Y. Yao, W. Jiang, M. Li, and W. P. Zhang, Effects of loss on the phase sensitivity with parity detection in an SU(1, 1) interferometer, J. Opt. Soc. Am. B **35**, 001080 (2018).
[56] M. O. Scully and M. S. Zubairy, *Quantum Optics* (Cambridge University Press, Cambridge, UK, 1997).
[57] H. Y. Fan and H. R. Zaidi, Application of IWOP technique to the generalized Weyl correspondence, Phys. Lett. A **124**, 303 (1987).
[58] H. Y. Fan, Newton-Leibniz integration for ket-bra operators in quantum mechanics (V): Deriving normally ordered bivariate-normal-distribution form of density operators and developing their phase space formalism, Ann. Phys. **323**, 1502 (2008).
[59] H. Y. Fan, H. L. Lu, and Y. Fan, Newton-Leibniz integration for ket-bra operators in quantum mechanics and derivation of entangled state representations, Ann. Phys. **321**, 480 (2006).
[60] B. M. Escher, R. L. de Matos Filho, and L. Davidovich, General framework for estimating the ultimate precision limit in noisy quantum-enhanced metrology, Nat. Phys. **7**, 406 (2011).
[61] S. K. Chang, W. Ye, H. Zhang, L. Y. Hu, J. H. Huang, and S. Q. Liu, Improvement of phase sensitivity in SU(1, 1) interferometer via a Kerr nonlinear, arXiv:2103.07844v1.